Case Studies in Construction Materials 16 (2022) e00856

Contents lists available at ScienceDirect

Case Studies in Construction Materials

journal homepage: www.elsevier.com/locate/cscm

Case study

Prefabricated UHPC-concrete-ECC underground utility tunnel reinforced by perforated steel plate: Experimental and numerical investigations

Bo-Tao Huang [a], Ji-Xiang Zhu [a], Ke-Fan Weng [a,b], Jun-Qi Huang [c,d,**], Jian-Guo Dai [a,*]

[a] *Department of Civil and Environmental Engineering, The Hong Kong Polytechnic University, Kowloon, Hong Kong, China*
[b] *Department of Ocean Science and Engineering, Southern University of Science and Technology, Shenzhen, Guangdong, China*
[c] *School of Civil and Hydraulic Engineering, Hefei University of Technology, Hefei, Anhui, China*
[d] *Prefabricated Building Research Institute of Anhui Province, Hefei, Anhui, China*

ARTICLE INFO

Keywords:
Ultra-High-Performance Concrete (UHPC)
Engineered Cementitious Composites (ECC)
Strain-Hardening Cementitious Composites (SHCC)Perforated steel plate
Underground structure
Utility tunnel
Digital Image Correlation (DIC)
Finite element analysis

ABSTRACT

In this study, perforated steel plate-reinforced utility tunnel with the use of ultra-high-performance concrete (UHPC) and engineered cementitious composite (ECC) was proposed. The mechanical performance of the composite utility tunnel was experimentally investigated, and the cracking behavior and failure process were analyzed based on the digital image correlation (DIC) technique. It was found that the crack-control (durability) performance of the composite utility tunnel was superior to that of concrete utility tunnel with the same reinforcement ratio, and the composite utility tunnel can be used in severe corrosive environment. Additionally, the composite action between perforated steel plate and ECC was evaluated based on direct tension test and DIC analysis. Finite element (FE) analysis was conducted on the perforated steel plate-reinforced ECC and composite utility tunnel for a comprehensive understanding of the mechanical behaviors. The findings of this study provided useful knowledge for the design and application of the proposed composite utility tunnel for underground construction.

1. Introduction

The proportion of the global urban population is expected to increase to 66% by 2050 [1]. The rapid urbanization (especially in developing countries) results in higher population density and larger pressure on the limited ground space for modern cities. As a result, increasing attention has been paid on underground construction to achieve a more effective utilization of urban space. One of the most common underground structures for modern cities is utility tunnel [2], which is a joint-use underground tunnel incorporating part or all of the urban utilities (e.g., water supply, electric power, gas, telecommunication, sewerage, heat supply, etc.). Taking Mainland China for example, it was reported that many of the major cities have constructed more than 100-km underground utility tunnels till 2020 [3].

---

[*] Corresponding author.
[**] Corresponding author at: School of Civil and Hydraulic Engineering, Hefei University of Technology, Hefei, Anhui, China.

E-mail addresses: botaohuang@zju.edu.cn (B.-T. Huang), ji-xiang.zhu@connect.polyu.hk (J.-X. Zhu), clusin.weng@connect.polyu.hk (K.-F. Weng), 2019800122@hfut.edu.cn (J.-Q. Huang), cejgdai@polyu.edu.hk (J.-G. Dai).

https://doi.org/10.1016/j.cscm.2021.e00856
Received 19 September 2021; Received in revised form 27 November 2021; Accepted 22 December 2021

According to the Chinese Standard GB50838-2015 [4], the service life of underground utility tunnels should be longer than 100 years. In addition, the maximum allowable crack width of the concrete layer of utility tunnels should be strictly controlled (i.e., 200 μm for common environment [4] and 150 μm for severe corrosive environment [5]). For underground utility tunnels, the durability of external parts exposed to complex underground environments [6] and the safety of internal parts under fire conditions [7] are two major concerns. Conventional underground utility tunnels are generally made by reinforced concrete. As a quasi-brittle material, ordinary concrete is easy to crack under tensile loadings and its spalling resistance under elevated temperature is a big concern when a high strength grade is used for enhanced durability. Hence, it remains a challenge regarding how to improve the durability and fire performance of the concrete structures of underground utility tunnels. In recent decades, significant research progress has been made in the development of advanced fiber-reinforced cement-based materials [e.g., Engineered Cementitious Composite (ECC) [8–10] and Ultra-High-Performance Concrete (UHPC) [11–14], which are promising in the construction of underground infrastructures with high performance and long-term durability.

Engineered cementitious composite (ECC) is a high-performance cement-based material featuring tensile strain-hardening and multiple-cracking characteristics [15–17]. ECC is also known as strain-hardening cementitious composites (SHCC) [18,19] or ultra-high toughness cementitious composites (UHTCC) [20,21]. For ordinary ECC materials, the compressive strength ranges from 20 to 80 MPa and the tensile strain capacity ranges from 1% to 6% [22–24]. Typically, the tensile crack of ECC is smaller than 100 μm and the autogenous healing of fine cracks can be observed in ECC materials [25–27]. The structural performance of ECC materials have been comprehensively investigated (e.g., [28–32]), and it was found that ECC can enhance the mechanical and durability performance of concrete members. In addition, no explosive spalling was observed in ECC during fire tests, and the mechanical performance of fire-damaged ECC is similar to or better than that of ordinary concrete materials [33–35].

Ultra-high performance concrete (UHPC) is a cement-based material featuring ultra-high compressive strength (typically $\geq$ 120 MPa [36]), high tensile strength, and excellent durability [11,12,36,37]. The addition of steel fibers in UHPC can achieve multiple cracking prior to crack localization and considerable energy absorption before fracture failure [12]. Additionally, UHPC shows significant lower water and chloride permeability compared to ordinary concrete materials. On the basis of the aforementioned excellent performance, UHPC can be employed as an exterior protective layer for reinforced concrete structures to improve both the mechanical performance and long-term durability.

Obviously, both ECC and UHPC have great potential in the application of high-performance and durable underground concrete structures. However, the costs of both materials are significantly higher than that of ordinary concrete. Hence, a cost-effective utilization of ECC and UHPC is critical for the widespread practical applications. On the basis of the concept of functionally-graded structures, the authors proposed a novel type of UHPC-Concrete-ECC underground utility tunnel (Fig. 1**a**) to address the durability and fire-resistance concerns [38]. In this design, UHPC is used as an exterior layer to protect the tunnel from the penetration of water and corrosive agents in soil environment; ECC is used as an interior layer to improve the crack-control capacity and fire resistance for the internal space; and ordinary concrete is used to fill the space between the two layers to minimize the thicknesses of ECC and UHPC. Perforated steel plate system (Fig. 1**b**) is applied to reinforce the three-layer functionally-graded structure. During the casting of concrete layers, ECC, UHPC and ordinary concrete can pass through the holes of steel plates and form “shear connectors” after hardening so as to ensure good composite performance between the steel plate and concrete materials. Additionally, such a reinforcing system forms a cage to ensure the integrity of the three-layer structure. It should be pointed out that the composite utility tunnel can be prefabricated for better quality control. In the previous study [38], the flexural performance of UHPC-concrete-ECC composite beam reinforced by perforated steel plate was experimentally investigated by the authors. It has been proven that the composite beam shows higher load capacity and superior crack-control capacity compared to the ordinary concrete one.

In this study, a UHPC-concrete-ECC composite utility tunnel was first fabricated, and its mechanical performance was experimentally investigated. A direct tension test was conducted to evaluate the composite performance of perforated steel plate-reinforced

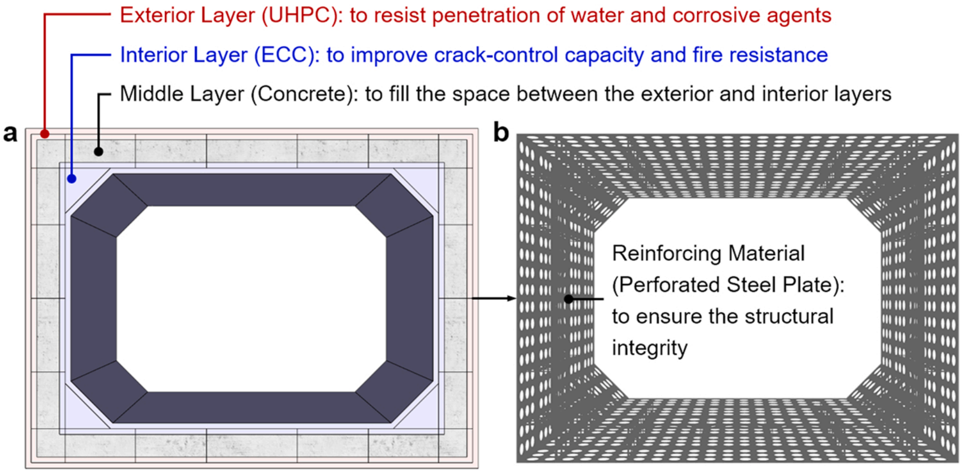

Fig. 1. Schematic of (a) UHPC-concrete-ECC composite utility tunnel and (b) perforated steel plate reinforcing system.

ECC, which was mainly under tension during the structural test. Digital image correlation (DIC) technique was used to monitor the strain field and to analyze the crack development during the tests. Furthermore, finite element (FE) modeling was carried out to reproduce the results of structural and tension tests for a comprehensive understanding of the mechanical performance of the composite utility tunnel.

2. Experimental programs

2.1. *Structural test of UHPC-concrete-ECC utility tunnel*

2.1.1. *Specimen dimensions*

To evaluate the mechanical performance of the proposed utility tunnel, one model with a hollow rectangular section (Fig. 2) was fabricated and tested, with the outer dimensions of 2000 mm × 1500 mm × 300 mm (length × height × depth) and the wall thickness of 200 mm^3 was fabricated and tested. It should be pointed out that the dimensions of the model utility tunnel were determined according to the available test equipment in the laboratory. The detailed dimensions of the specimen are presented in Fig. 2. The dimensions of the specimen section were 300 × 200 mm^2. The thicknesses of UHPC, concrete, ECC and perforated steel plate were 50 mm, 100 mm, 50 mm and 1 mm, respectively. The diameter of the holes of the steel plates was 50 mm. Four longitudinal perforated steel plates were welded to form the external loop reinforcement (2 A+ 2 C) and inner loop (2B+2D) reinforcement, respectively (see Fig. 2), and a series of transverse perforated steel plates (12E+10E) were connected through welding with the two loops to form a three dimensional cage of reinforcement of the tunnel, which four corners were also enhanced with four diagonal plates (4 F) (see Fig. 2). All the longitudinal perforated steel plates had an opening area of 24% [i.e., (A), (B), (C), and (D) of Fig. 2]. For all the steel plates, the smallest width of perforated section (i.e., excluding the hole width) was the same, which was 50% of that of the section without any holes. It should be pointed out that the longitudinal steel plates were located in the middle of the UHPC and ECC layers and their cover thickness was 25 mm.

2.1.2. *Fabrication process*

The fabrication process of the utility tunnel specimen includes five steps (Fig. 3). First, timber formworks were prepared for the outer and inner perimeters of the tunnel. The welded cage of reinforcement system was then fixed in the timber formwork. Second, form boards were used to fill in the gap between two loop reinforcements. Third, the UHPC and ECC layers were cast into the formwork and cured for 14 days. Fourth, the fillers between UHPC and ECC layers were removed. Finally, C30 commercial concrete was cast into the formwork and cured for 28 days, and the timber formwork was then removed.

2.1.3. *Testing methods*

The test setup for the utility tunnel specimens is presented in Fig. 2. Three hydraulic actuators were used in the test. Two actuators were located at the center of two side walls of the utility tunnel to simulate the soil pressure. The last actuator was used to exert flexural load on the top wall through a transfer beam, with a 300 mm constant moment zone. The load steps during the structural test are listed in Table 1, and the loads applied by the two lateral actuators were the same. In addition, the loads of the actuators are graphically represented in Fig. 4 for better understanding. It should be pointed out that the load at step No. 7 corresponds to the design load, which was estimated upon the condition that the thickness of covering soil is 3000 mm (from the top surface of tunnel to the ground) and traffic loads are assumed to be 100 kN/m^2 according to Chinese Standard GB50009-2019 [39]. After the design load, the applied loads increased until the failure occurred. The holding time was 3 min for Load step No. 1–7, and was 5 min for step No. 8–26. As presented in Fig. 2, linear variable differential transformers (LVDTs) were used to monitor the displacements at different positions of the tested utility tunnel based on the principle of symmetry.

Digital Image Correlation (DIC) Analysis. As an optical-based non-contact method, DIC can measure the displacement and strain fields on the specimen surface. DIC analysis has been successfully applied in the monitoring of the cracking process of ECC materials [40,41] and ECC-strengthened concrete members [42,43]. In the structural test of the utility tunnel, DIC was used to monitor the central part of the top wall with an area of 500 × 200 mm^2 (see Fig. 2), in which speckle pattern was applied onto the surface. During the test, two light sources were used to highlight the patterned area, and a digital camera was used to take digital photographs at the end of each load step (see Table 1). In the digital photographs, the resolution of the patterned area was 855 × 342 pixels corresponding to 500 × 200 mm^2 on physical scale. In DIC post-processing, a subset size of 60 pixels and a step size of 15 pixels was used.

2.2. *Tensile test of perforated steel plate-reinforced ECC (ST-ECC)*

According to the moment distribution of the tested utility tunnel, the UHPC layer was in compression and the ECC layer was in tension at the central parts of the top and side walls. In such a case, the tensile failure of the ECC layer is prior to the compressive failure of the UHPC layer, owing to the ultra-high compressive strength of UHPC. Thus, an experimental investigation on the tensile performance of perforated steel plate-reinforced ECC (ST-ECC) is essential and helpful to understand the structural performance of the utility tunnel.

2.2.1. *Specimen preparation*

Two identical specimens with dimensions of 480 × 100 × 50 mm^3 were prepared for the direct tension test (see Fig. 5) to assess the tension stiffening effect of ST-ECC. This testing method has been successfully utilized for the monotonic and cyclic tensile tests of ECC

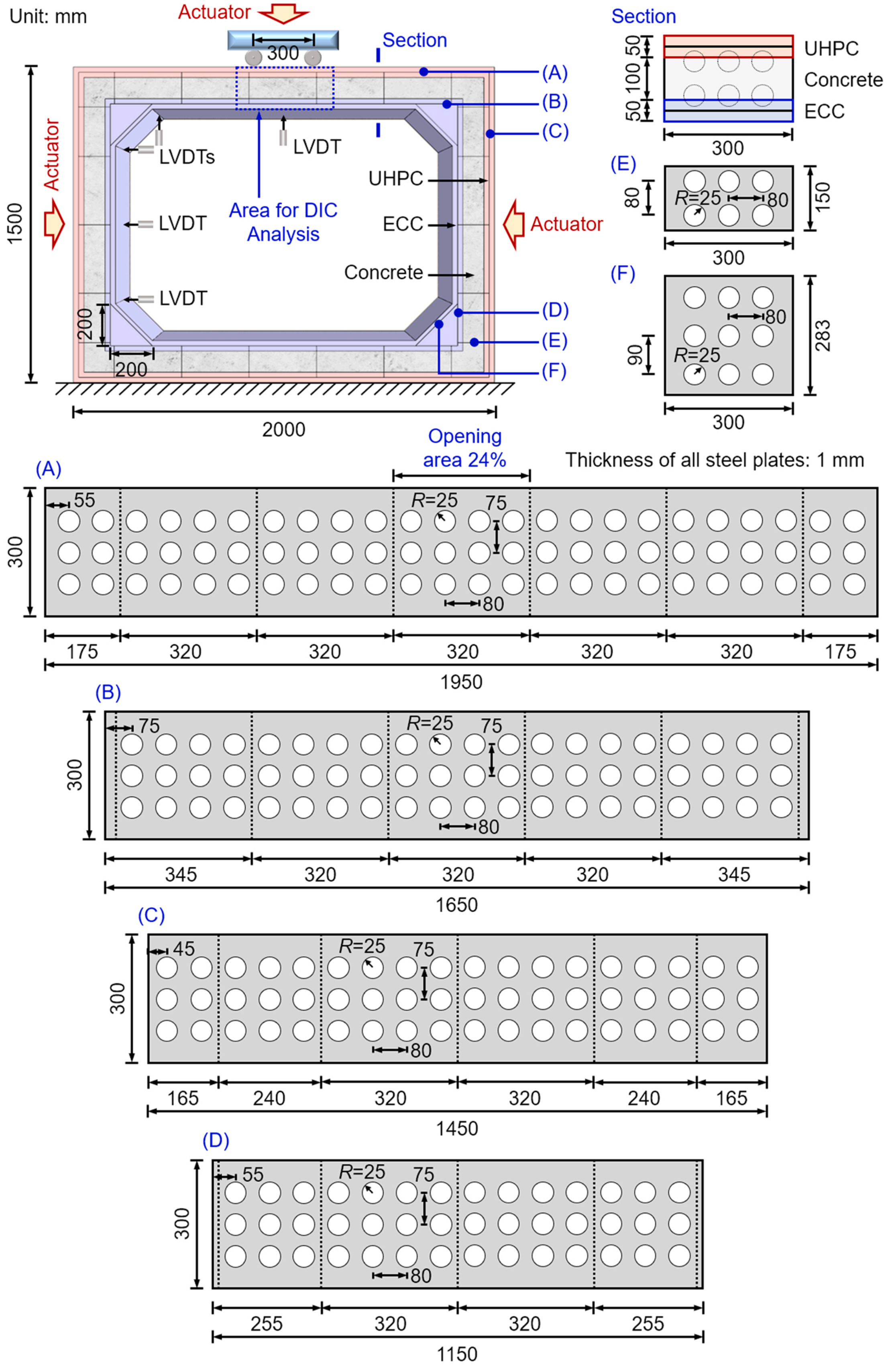

(caption on next page)

Fig. 2. Dimensions and test setup of the UHPC-concrete-ECC composite utility tunnel.

materials [24]. For the perforated steel plate in Fig. 5, the smallest section (50% of the section without hole), opening area (24%), and thickness (1 mm) are the same with those of the steel plates (A)~(D) in Fig. 2. The thickness of ECC (50 mm) is also the same with that in Fig. 2. To evaluate the composite effect of ST-ECC, direct tension tests were also conducted on the perforated steel plate and ECC individually (see Fig. 5).

2.2.2. *Testing methods*

The tensile tests were conducted using a 1000-kN INSTRON™ system. The loading rate was the same for all the specimens (0.5 mm/min), and LVDTs were used to measure the tensile displacement with a gauge length of 320 mm.

2.2.3. *Digital image correlation (DIC) analysis*

The central parts of the ST-ECC and ECC specimens were monitored using DIC and the speckle pattern was applied (see Fig. 5). During the test, a digital photograph was taken every 3 s. The resolution of the patterned area was 755 × 118 pixels corresponding to 320 × 50 mm^2 on physical scale. In DIC post-processing, GOM Correlate Software [44] was used with a subset size of 80 pixels and a step size of 5 pixels.

2.3. *Material properties*

In this section, the mechanical properties of ECC, UHPC, ordinary concrete and perforated steel plate will be briefly presented and more details about the raw materials can be found in the authors' previous work [38].

2.3.1. *ECC*

The matrix proportion of ECC was as follows (kg/m^3): cement: silica fume: sand: water: super-plasticizer = 912: 228: 342: 467: 5. Polyethylene (PE) fiber (1.5 vol%) was used in the preparation of ECC. The 28-day compressive strength and modulus of ECC were 54.0 MPa and 18 GPa, respectively. The 28-day tensile strain capacity of ECC cuboid specimen (Fig. 5) was 2.4% with the tensile strength of 3.0 MPa.

2.3.2. *UHPC*

The matrix proportion of UHPC was as follows (kg/m^3): cement: silica fume: sand: water: super-plasticizer = 1160: 290: 435: 290: 20. Steel fiber (2.0 vol%) was used in the preparation of UHPC. The 28-day compressive strength and modulus of UHPC were 125.0 MPa and 39 GPa, respectively. The 28-day tensile strain capacity of UHPC was 0.5% with the tensile strength of 7.5 MPa.

2.3.3. *Ordinary concrete*

In this study, C30 commercial concrete was used and the diameters of its coarse aggregates were smaller than 10 mm, so as to

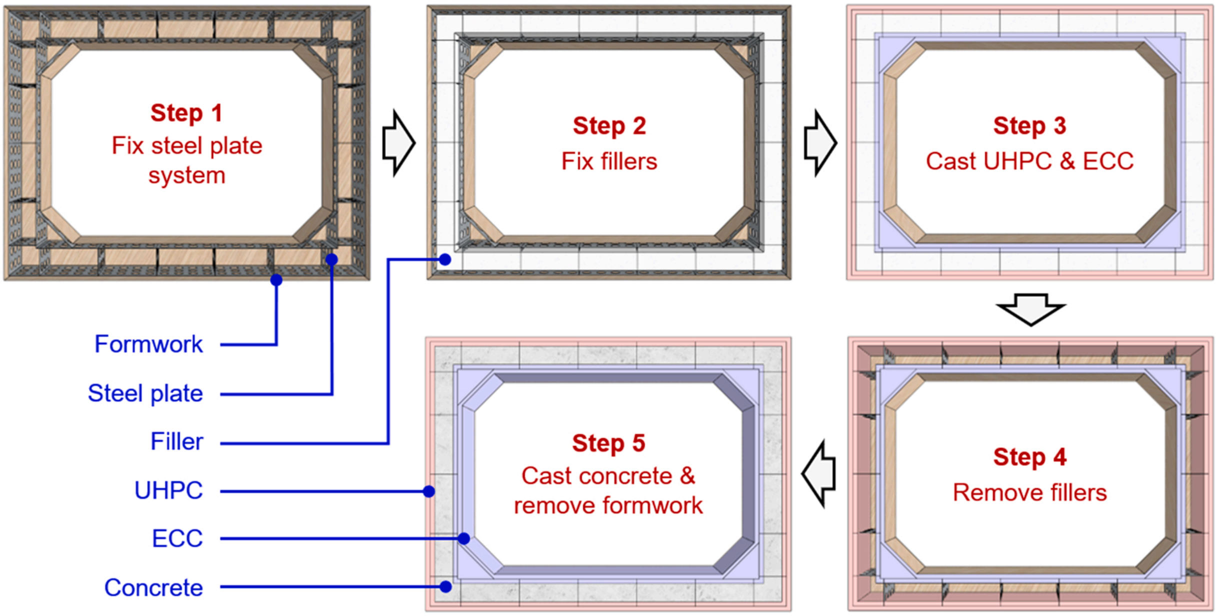

Fig. 3. Fabrication process of the utility tunnel specimen.

ensure the concrete could easily pass through the holes (diameter of 50 mm) of the steel plates. The 28-day cylinder compressive strength of the concrete material was 22.8 MPa.

2.3.4. Perforated steel plate

For all the perforated steel plate in this study, the thickness was 1 mm and the diameter of the holes was 50 mm. The yield stress of steel plate was 190 MPa with the yield strain of 0.1%, and the ultimate strength was 310 MPa with the strain of 25%.

3. Results on tensile performance of ST-ECC

The tensile performance of the perforated steel plate, ECC cuboid, and ST-ECC are presented in Fig. 6**a**, **b**, and **c**, respectively. It should be pointed out that the average strain is calculated based on the deformations within the 320-mm test length between two clamping ends in Fig. 5, and the stress is the average stress of the specimen sections (50×1 mm^2 for steel plate, and 100×50 mm^2 for ECC cuboid and ST-ECC).

In Fig. 6**a**, it can be observed that most of the deformation is attributed to the weak region around the holes of the steel plate. The tensile performance of ECC cuboid is presented in Fig. 6**b**, and ECC-avg means the average response of two specimens with the strain capacity of 2.4% and strength of 3.0 MPa. In Fig. 6**c**, the tensile curves of ST-ECC are shown and ST-ECC-avg represents the average response. The estimated tensile curve (gray solid line in Fig. 6**c**) is obtained by directly superimpose the tensile curve of steel plate in Fig. 6**a** and ECC-avg in Fig. 6**b**. It can be found that the estimated tensile curve is significantly higher than the tested one. This phenomenon will be explained in the following. In Fig. 6**d**, the estimated tensile behavior of ECC in ST-ECC is presented, which is obtained by subtracting the tensile curve of steel plate in Fig. 6**a** from ST-ECC-avg in Fig. 6**c**. It can be seen that the curve of ECC in ST-ECC is significantly lower than the average tensile curve of ECC cuboid (i.e., ECC-avg Fig. 6**d**). Actually, the in-situ tensile contribution of ECC is strongly influenced by the mechanical interaction between the ECC and the perforated steel plate and the strain localization of the latter influences the stress development in the former. In addition, the strain capacity of ST-ECC corresponding to the peak tensile stress in Fig. 6**c** is governed by the deformability of ECC, as the ultimate strain of the steel plate is much larger than that of ECC. The above arguments will be further proven based on the DIC results in the following.

The DIC results of the ECC cuboid and ST-ECC at three tensile strain levels (0.1%, 1.0%, and 2.0%) are presented in Fig. 7. It should be pointed out that the strain field around relatively large cracks could not be analyzed by DIC. For ECC cuboid in Fig. 7**a**, the fine cracks uniformly distributed along the tensile direction and the major crack could not be distinguished from the multiple cracks. For ST-ECC in Fig. 7**b**, significant strain localization can be observed, especially around the holes of the steel plate (marked by the dashed lines). The strain localization resulted in the fact that compared to ECC cuboid (Fig. 7**a**), saturated cracking of ECC in ST-ECC (Fig. 7**b**) could not be achieved and the in-situ tensile strength of ECC layer would be lower than its material strength, which explains why the tested tensile performance of ST-ECC was lower than the estimated one (Fig. 6**c**). This experimental finding is important for the adjustment of in-situ tensile constitutive model of the ECC layer in Section 6.

4. Experimental results of composite utility tunnel

4.1. DIC results and failure process

The mid-span load-deflection curve of the top wall of the utility tunnel is shown in Fig. 8. Five load steps of the top hydraulic actuator (0, 36 kN, 52 kN, 64 kN, and 82 kN) are marked in Fig. 8, which correspond to point A, B, C, D, and E, respectively. At the ultimate stage (point E), the load of the top hydraulic actuator was 82 kN. On the basis of DIC analysis, the strain field of point A to D are presented in Fig. 8. However, as the load capacity of the utility tunnel was much higher than the estimation prior to test, the battery of DIC camera ran out after load step No. 17 (64 kN, point D). Hence, the cracks of the top wall at the ultimate stage (point E) were drawn based on the photographs recorded by another camera. In Image B (36 kN) of Fig. 8, the cracks can be observed in the ECC layer and along the steel plates. As the load increases, more significant cracking behavior can be observed in these regions (see Image C and D of Fig. 8). At the ultimate stage (Image E), multiple cracking of the ST-ECC layer can be clearly observed, and the ECC/concrete and UHPC/concrete interface cracks can be also seen. It should be noted that the failure of the top wall was governed by the shear failure of the concrete layer. According to the DIC result, the tensile strain of the steel plate in ECC at point E was approximately 0.08% (not

Table 1
Load steps of the structural test.

Load step & actuators	Load (kN)								
Load step No.	**0**	**1**	**2**	**3**	**4**	**5**	**6**	**7**	**8**
Top actuator	0	6.0	12.0	18.0	23.0	28.0	32.0	36.0	40.0
Lateral actuators	0	4.0	8.0	12.0	16.0	19.0	21.0	23.0	25.0
Load step No.	**9**	**10**	**11**	**12**	**13**	**14**	**15**	**16**	**17**
Top actuator	43.0	46.0	49.0	52.0	54.0	56.0	58.0	62.0	64.0
Lateral actuators	26.5	28.0	29.5	31.0	32.0	33.0	34.0	36.0	37.0
Load step No.	**18**	**19**	**20**	**21**	**22**	**23**	**24**	**25**	**26**
Top actuator	66.0	68.0	70.0	75.0	75.0	77.0	80.0	82.0	71.0
Lateral actuators	38.0	39.0	39.0	39.0	39.0	39.0	39.0	39.0	39.0

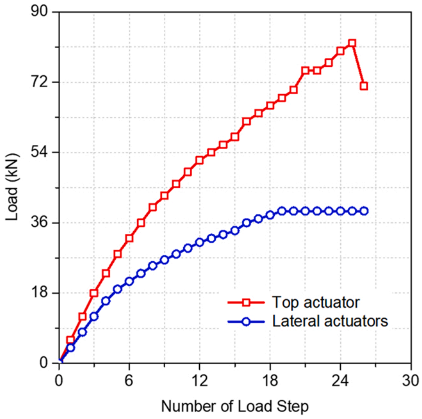

Fig. 4. Loads of the top and lateral actuators during the structural test.

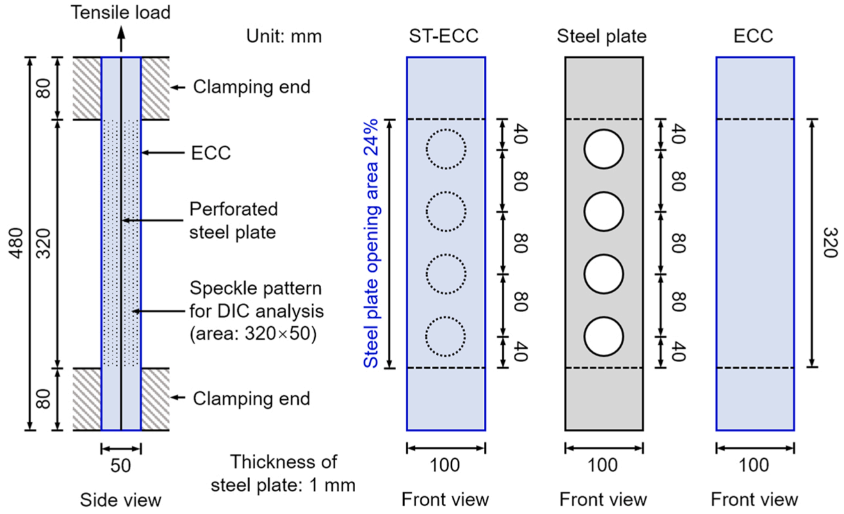

Fig. 5. Test setup for ECC panel reinforced with perforated steel plate.

yielded).

4.2. Deflection of composite utility tunnel

The deflection of the composite utility tunnel at different load levels (top hydraulic actuator) are presented in Fig. 9, which were measured by the LVDTs at various locations. It should be noted that the right and bottom axes of Fig. 9 represent the deflections of the top wall and one side wall, respectively. As the load increased, the deflection of the composite utility tunnel increased. At the design load (load step No. 7, 36 kN), the mid-span deflection of the top wall (0.66 mm, measured by LVDT 1) was 1/1894 of the net span (1250 mm), and the maximum deflection of the side wall (0.29 mm, measured by LVDT 3) was 1/2586 of the net span (750 mm). At the load step No. 23 (77 kN), the mid-span deflection of the top floor (2.96 mm) was 1/422 of the net span, and the maximum deflection of the side wall (1.08 mm) was 1/694 of the net span. In summary, the deflection of the composite utility tunnel was relatively small. It should be pointed out that after 77 kN, LVDT 2–4 were removed for safety reason and only LVDT 1 kept working.

4.3. Crack width development

According to the method provided in [42], the crack widths of concrete member can be measured based on DIC analysis. For the top wall of the composite utility tunnel, the development of the maximum crack width is plotted in Fig. 10. In addition, the section of a reinforced concrete (RC) member (C30 concrete) is also presented, whose dimensions and tension reinforcement ratio (0.25%, 3Φ8) are the same with those of the composite utility tunnel. For the sake of comparison, the development of the maximum crack width of the RC member is calculated under the same loading and support conditions with that of the composite utility tunnel, according to Chinese Standard GB50010-2010 [45]. It can be seen that compared to the RC member with the same section and reinforcement ratio, the maximum crack width of the UHPC-concrete-ECC member in the utility tunnel is smaller at all the load levels. As mentioned in Section 1, the maximum allowable crack width of the concrete layer of utility tunnels needs to be strictly controlled (i.e., 200 μm for mild environment [4] and 150 μm for severe corrosive environment [5]). These two limit values are also plotted in Fig. 10. It can be seen that for the case of 150 μm, the load of RC member is around 36 kN (the design load in this study), while the corresponding load in the composite utility member is around 42 kN (17% higher compared to the RC member). For the case of 200 μm, the load of RC member is around 50 kN, while that of the composite utility member is around 61 kN (22% higher compared to the RC member). Thus, in terms of crack-control (durability) performance, the proposed composite utility tunnel is superior to conventional RC utility tunnel with the same dimensions and reinforcement ratio, and it can be used in severe corrosive environment.

5. Finite element (FE) analysis

A three-dimensional (3D) FE analysis was conducted based on the general-purpose FE software ABAQUS [46] to simulate the mechanical behavior of the ST-ECC and composite utility tunnel, aiming to facilitate a better understanding on their structural performance and to propose a general model for further investigation. Details of the FE models and the analysis results are presented in the following.

5.1. *Material constitutive models*

The steel plate was modeled using the isotropic material with Von Mises yield criteria and a bi-linear model [47] was used [i.e., Eq. (1)]. The yield strain (ε_y) and yield strength (f_y) are 0.1% and 190 MPa, respectively; the ultimate strain (ε_u) and ultimate strength are 25% and 310 MPa, respectively; and the Poisson's ratio is 0.30.

$$\sigma_s = \begin{cases} E_s\varepsilon\left(0 \le \varepsilon \le \varepsilon_y\right) \\ f_y + E_u\left(\varepsilon - \varepsilon_y\right)\left(\varepsilon_y < \varepsilon \le \varepsilon_u\right) \end{cases} \tag{1}$$

The damage plasticity model was used for ECC, UHPC, and ordinary concrete. For the compressive behavior of ECC, the constitutive

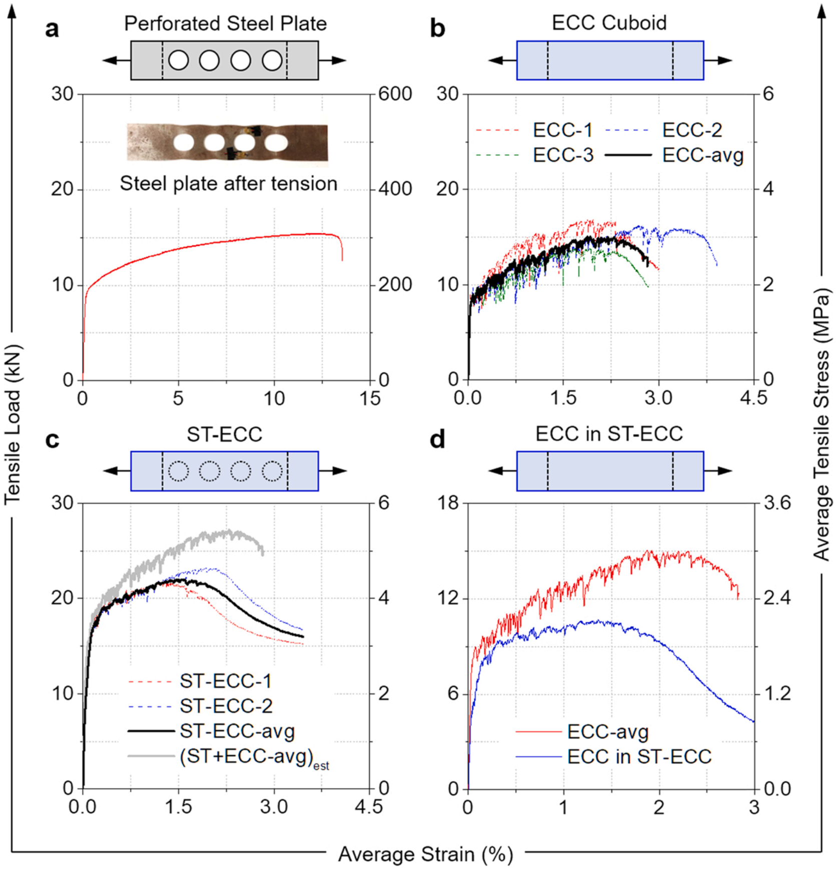

Fig. 6. Tensile performance of (a) perforated steel plate, (b) ECC cuboid specimen, (c) perforated steel plate-reinforced ECC (ST-ECC), and (d) ECC layer in ST-ECC. The in-situ tensile strength of ECC layer in ST-ECC is lower than that of ECC cuboid.

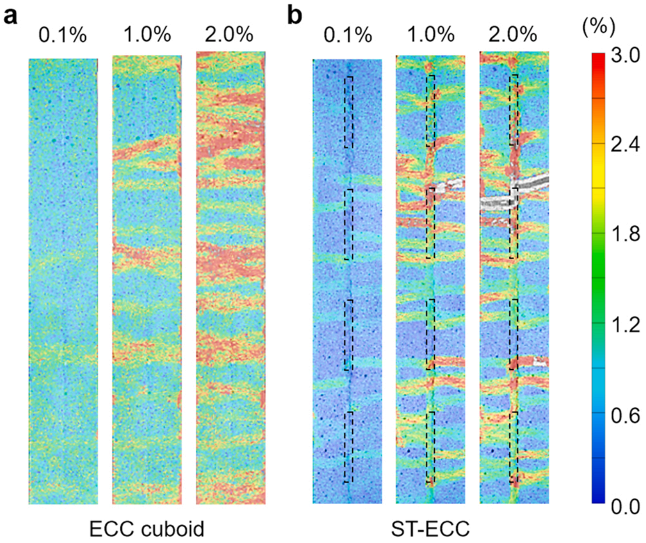

Fig. 7. DIC results of (a) ECC cuboid and (b) ST-ECC. The existing of perforated steel plate results in more significant crack localization of ST-ECC compared to ECC cuboid.

model proposed by Zhou et al. [22] (Fig. 11**a**) was used to model the stress-strain relationship [i.e., Eq. (2)].

$$\sigma_E = \begin{cases} E_E\varepsilon & (0 \le \varepsilon \le \varepsilon_{Ec1}) \\ E_E\varepsilon[(1 - aE_E\varepsilon)/\sigma_{Ec2} + b] & (\varepsilon_{Ec1} < \varepsilon \le \varepsilon_{Ec2}) \\ (\sigma_{Ec2} - \sigma_{Ec3})(\varepsilon - \varepsilon_{Ec2})/(\varepsilon_{Ec2} - \varepsilon_{Ec3}) + \sigma_{Ec2} & (\varepsilon_{c2} < \varepsilon \le \varepsilon_{c3}) \\ (\sigma_{Ec3} - \sigma_{Ec4})(\varepsilon - \varepsilon_{Ec3})/(\varepsilon_{Ec3} - \varepsilon_{Ec4}) + \sigma_{Ec3} & (\varepsilon_{Ec3} < \varepsilon \le \varepsilon_{Ec4}) \end{cases} \tag{2}$$

where E_{E} is the elastic modulus of ECC (18 GPa); *a* and *b* are constant parameters, which are taken as 0.308 and 0.124, respectively; $\varepsilon_{\mathrm{Ec1}}$, $\varepsilon_{\mathrm{Ec2}}$, $\varepsilon_{\mathrm{Ec3}}$ and $\varepsilon_{\mathrm{Ec4}}$ are 0.120%, 0.465%, 0.698%, and 4.186%, respectively; and σ_{Ec1}, σ_{Ec2}, σ_{Ec3} and σ_{Ec4} are 21.6 MPa, 54.0 MPa, 27.0 MPa and 0, respectively. The Poisson's ratio of ECC is 0.17.

The stress-strain relation of ECC, UHPC and concrete in tension was assumed to be linear elastic before cracking. The crack-bridging constitutive relation can be used in the modeling of their post-cracking tensile behavior. In this study, the tri-linear model as shown in Fig. 11**b** was used to simplify and model the crack-bridging constitutive relation of ECC. The parameters of this constitutive relation are listed in Table 2, which are determined based on the experimental results reported in the relevant literature [48,49]. Remember that the in-situ tensile strength of ECC was lower than its material strength, which was mentioned in Section 4. Thus, the peak stress (i.e., σ_{Et2} in Fig. 11**b**) is set to the same value as the in-situ tensile strength of ECC (i.e., 2.1 MPa, see Fig. 6**d**). Note that the validity of such an adjustment will be proven by the FE result in the following.

The compressive stress-strain model of UHPC is presented in Fig. 6**c**, which was proposed by Association Française du Génie Civil

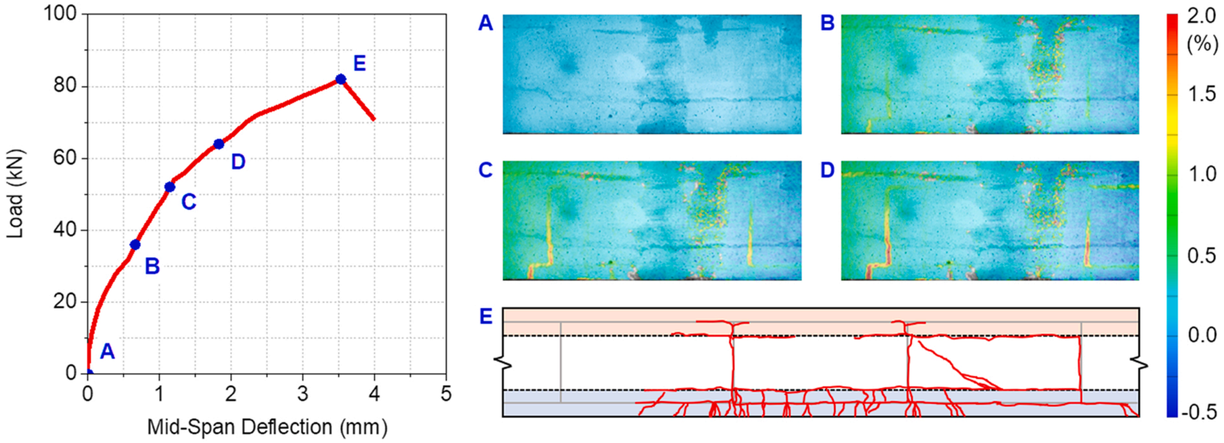

Fig. 8. Mid-span load-deflection curve and failure process of the top wall of the composite utility tunnel. The failure of the top floor is governed by the shear failure of concrete layer.

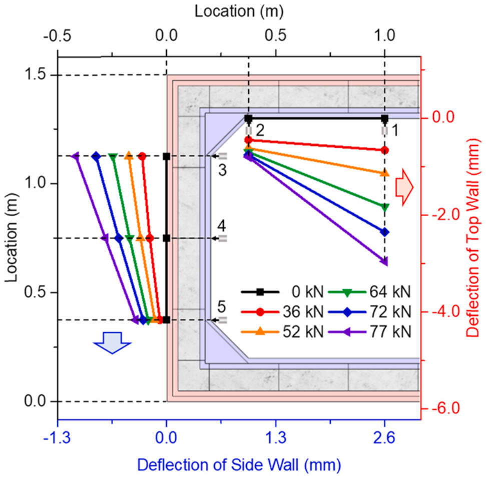

Fig. 9. Deflections of top floor and side walls at different load levels.

(AFGC) [50]. The first linear-elastic part is determined by the compressive strength and modulus of UHPC ($\varepsilon_{\mathrm{Uc1}} = 0.32\%$ and $\varepsilon_{\mathrm{Uc1}} = 125.0$ MPa). For the tested utility tunnel, the tensile failure of ECC was prior to the compressive failure of UHPC, owing to the ultra-high compressive strength of UHPC. Hence, the plastic plateau and softening stage in Fig. 6**c** were not considered in the FE analysis. The post-cracking tensile behavior of UHPC was modeled by the tri-linear crack-bridging relation (Fig. 6**d**), because the UHPC in this study also showed tensile strain-hardening behavior. The parameters of this tri-linear relation are listed in Table 2, which are determined based on the results in this study and the relevant literature [47,49]. The Poisson's ratio of UHPC is 0.22.

The compressive behavior of ordinary concrete was modeled with the Hognestad parabola curve (Fig. 6**e**), which can be expressed as Eq. (3) [51].

$$\sigma_c = \sigma_{Cc1}\left[2\left(\frac{\varepsilon}{\varepsilon_{Cc1}}\right) - \left(\frac{\varepsilon}{\varepsilon_{Cc1}}\right)^2\right] \tag{3}$$

where σ_{Cc1} is the compressive strength of ordinary concrete (22.8 MPa) and $\varepsilon_{\mathrm{Cc1}}$ (0.19%) is the strain at σ_{Cc1}. The value of $\varepsilon_{\mathrm{Cc1}}$ is determined based on the suggestions in the relevant literature [51]. The post-cracking tensile behavior was modeled with the bi-linear model in Fig. 6**e** and the parameters are listed in Table 2, which are determined based on the suggestions in the relevant literature [51]. The Poisson's ratio of concrete is 0.20.

For the other parameters of ECC, UHPC and concrete, the material dilation angle, the shape factor for the yield surface, the eccentricity parameter, and the ratio of initial equibiaxial compressive yield stress to initial uniaxial compressive yield stress were taken as 30°, 0.667, 0.1, and 1.16, respectively [52].

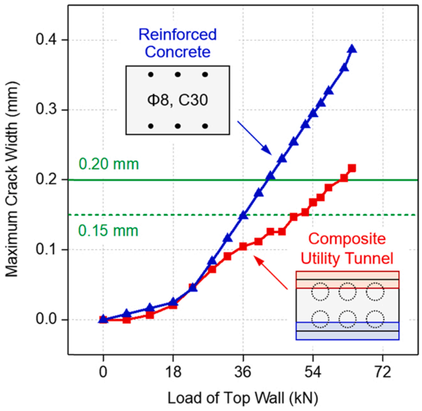

Fig. 10. Crack width development of the top wall of the composite utility tunnel. At the same load level, the maximum crack width of the composite utility tunnel is smaller than that of conventional concrete utility tunnel with the same dimensions and reinforcement ratio.

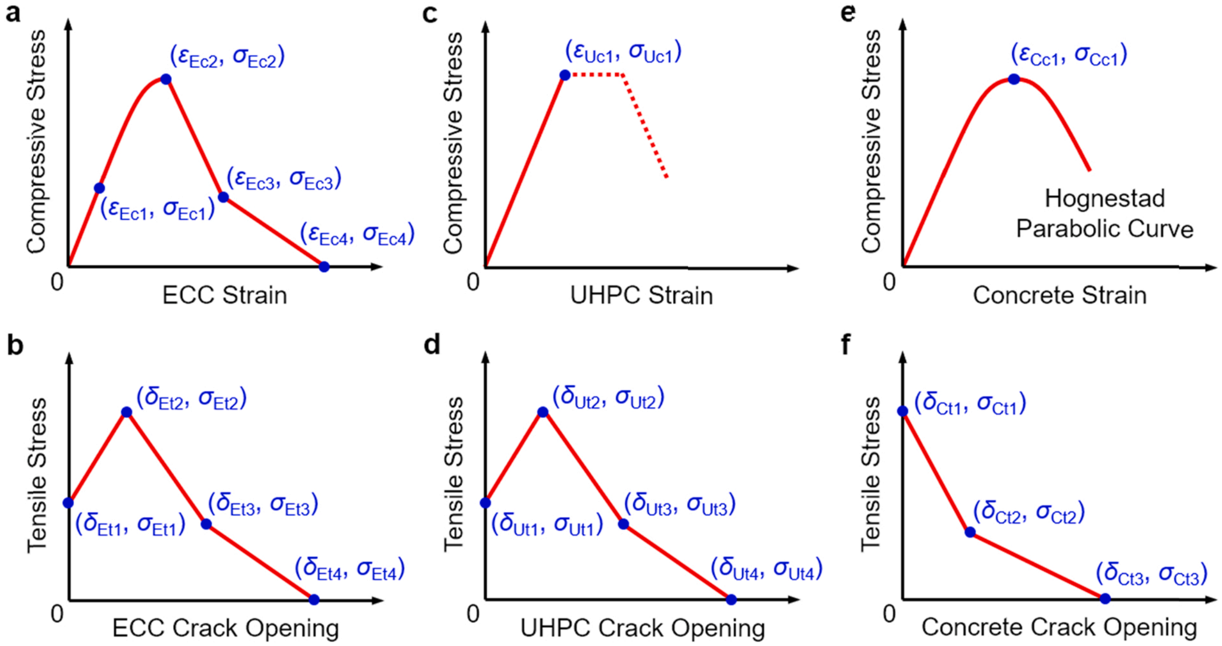

Fig. 11. Constitutive models of ECC, UHPC and concrete in FE analysis.

Table 2
Parameters in tensile post-cracking models of ECC, UHPC and concrete.

ECC	Values	UHPC	Values	Concrete	Values
Modulus	18 GPa	Modulus	39 GPa	Modulus	26 GPa
δ_{Et1}	0	δ_{Ut1}	0	δ_{Ct1}	0
σ_{Et1}	1.0 MPa	σ_{Ut1}	5.0 MPa	σ_{Ct1}	1.6 MPa
δ_{Et2}	0.18 mm	δ_{Ut2}	0.05 mm	δ_{Ct2}	0.02 mm
σ_{Et2}	2.1 MPa	σ_{Ut2}	7.5 MPa	σ_{Ct2}	0.53 MPa
δ_{Et3}	1.1 MPa	δ_{Ut3}	2.00 mm	δ_{Ct3}	0.11 mm
σ_{Et3}	0.50 mm	σ_{Ut3}	3.0 MPa	σ_{Ct3}	0
δ_{Et4}	1.50 mm	δ_{Ut4}	6.50 mm	/	/
σ_{Et4}	0	σ_{Ut4}	0	/	/

5.2. Perforated steel plate-reinforced ECC

The 3D FE model of ST-ECC is presented in Fig. 12. Eight-node brick element with reduced integration (C3D8R) was used to model the ECC and clamping ends, and four-node general-purpose shell element (S4R) was used to model the perforated steel plate. The adopted element size is 10 mm based on a convergence study, which can ensure a quick computation and continuous strain contour. It should be pointed out that the clamping ends were assumed to be linear elastic. The perforated steel plate was constrained in the ECC by using the "embedded region" function in ABAQUS, for which a perfect bond between the concrete and steel plate was assumed. A tie constraint was employed to make the translational and rotational motions equal for the surfaces of ECC and clamping ends. The nodes of the clamping ends at the right side were restrained in all translational degrees of freedom. For the clamping ends at the left side, all translational degrees of freedom were coupled to a reference point A (Fig. 12). The static analysis mode was used and the tensile load was applied at point A in a displacement control manner.

The results of FE analysis for tensile performance of ST-ECC are presented in Fig. 13. The simulated tensile stress-strain curve is close to that of the tested one (Fig. 13**a**). The FE model can provide reasonably accurate prediction of the initial stiffness and the load capacity, which validates the effectiveness of the peak-stress adjustment of the ECC tensile model (i.e., σ_{Et2} in Fig. 11**b**) according to the in-situ tensile strength of ECC. It should be pointed out that if such an adjustment was not conducted, the predicted load response of ST-ECC would be significantly higher than the tested one. The principal strain fields at the average strain of 2% are shown in Fig. 13**b**. For the ST-ECC, the strain concentration can be observed in the FE result and the simulated failure mode is similar to the tested one. Additionally, the deformation of the perforated steel plate in ST-ECC is also close to the experimental observation (Fig. 6**a**). The above FE results indicate that the employed model can be applied to predict the tensile behavior of ST-ECC.

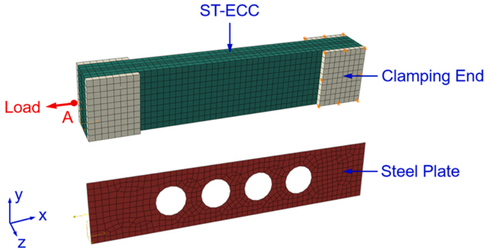

Fig. 12. FE model of ST-ECC.

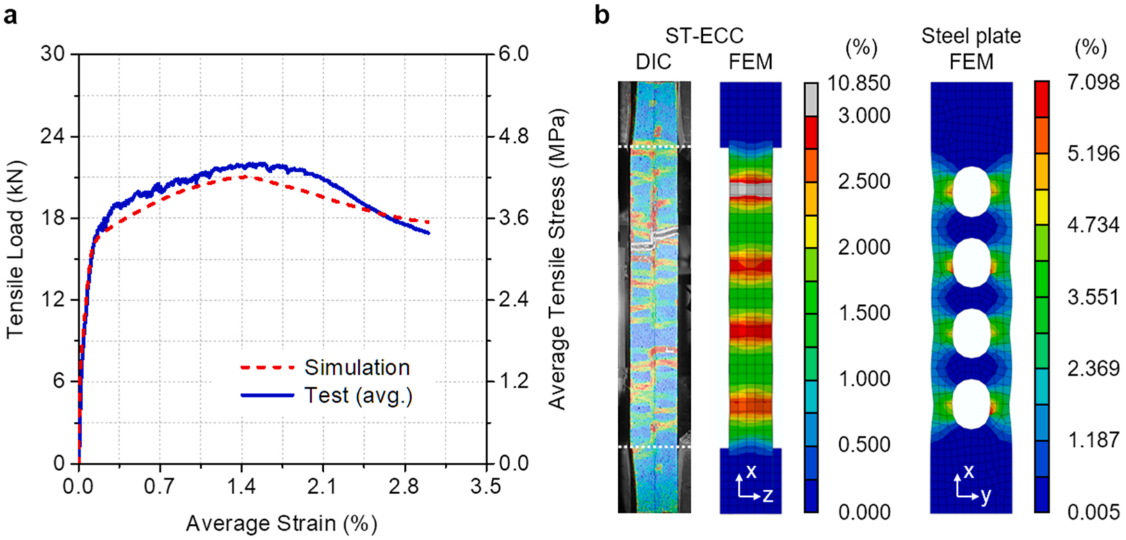

Fig. 13. Results of FE analysis for tensile performance of ST-ECC: (a) Tensile stress-strain curve and (b) principal strain fields at the average strain of 2%. The FE results show good agreement with the test results.

5.3. *Composite utility tunnel*

The 3D FE model in Fig. 14 is a quarter of the composite utility tunnel, which is symmetrical about the *xy*-plane and *yz*-plane. The *z*-dimensional thickness of the FE model is 150 mm (half of the tested utility tunnel depth, 300 mm). Eight-node brick element (C3D8R) was used to model the ECC, UHPC, concrete and loading pads [53], and four-node shell element (S4R) was used to model the perforated steel plates. The loading pads were assumed to be linear elastic. The *x*- and *z*-directional mesh lengths were 35 mm and the *y*-directional mesh lengths were 25 mm. The above mesh lengths were determined based on the simulation results and suggestions in the relevant literature [51,54]. According to the aforementioned FE result of ST-ECC, the perforated steel plate was also constrained in the ECC, UHPC, and concrete by using the “embedded region” function in ABAQUS. A tie constraint was employed to make the translational and rotational motions equal for the surfaces of ECC and loading pads. The nodes of the bottom of the model were restrained in all translational degrees of freedom. Symmetry constraints were used for the *xy*- and *yz*-planes. The static analysis mode was used in the FE analysis. The load on the side wall was applied in a force control manner, while the load on the top wall was applied in a displacement control manner and the analysis was terminated after the reaction force reached the peak value.

The traction-separation constitutive model in Fig. 15 were used to simulate the interface cohesive behavior between concrete and ECC/UHPC. This bi-linear traction-separation model assumes linear elastic behavior up to the maximum traction and the traction starts to decrease afterwards. In Fig. 15, τ_{n0}, τ_{s0} and τ_{t0} are the maximum tractions in normal, shear and tangent directions, respectively. The interface behavior before the damage initiation can be expressed as follows.

$$T = \begin{bmatrix} \tau_n \\ \tau_s \\ \tau_t \end{bmatrix} = \begin{bmatrix} \kappa_{nn} & 0 & 0 \\ 0 & \kappa_{ss} & 0 \\ 0 & 0 & \kappa_{tt} \end{bmatrix} \begin{bmatrix} \delta_n \\ \delta_s \\ \delta_t \end{bmatrix} = K\delta \tag{4}$$

where τ_n, τ_s and τ_t are the traction (***T***) components in normal, shear and tangent directions, respectively; k_{nn}, k_{ss} and k_{tt} are their elastic stiffnesses (***K***); and δ_n, δ_s and δ_t are the corresponding interface deformations (***δ***). It should be noted that very limited information on the interfacial behavior between concrete and ECC/UHPC was available. Therefore, in this study, δ_f (the maximum slip in Fig. 15) was assumed to be 20 mm according to the suggestion in [54]. k_{nn}, k_{ss}, and k_{tt} were assumed to be equal [55] and the value was

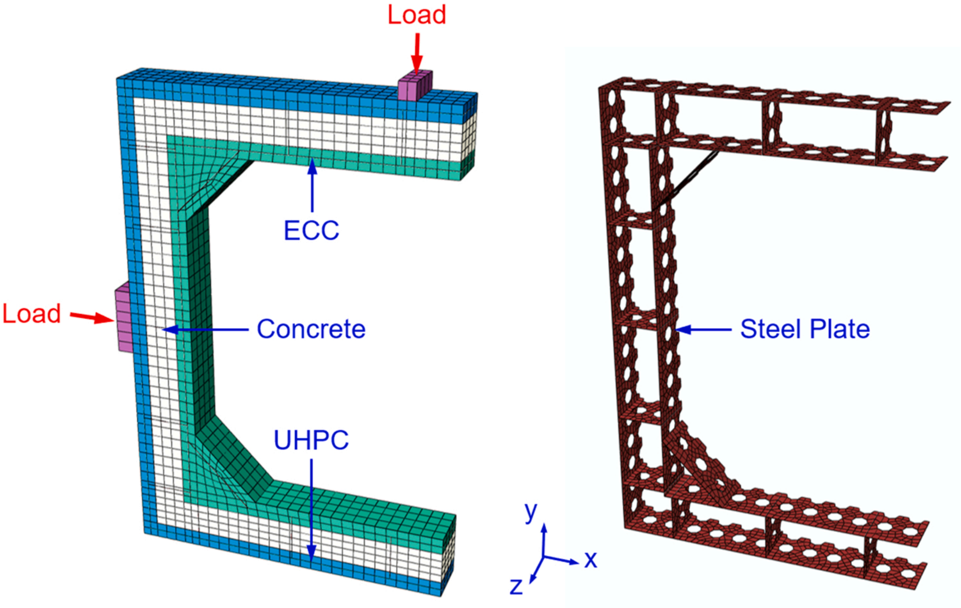

Fig. 14. FE model of composite utility tunnel.

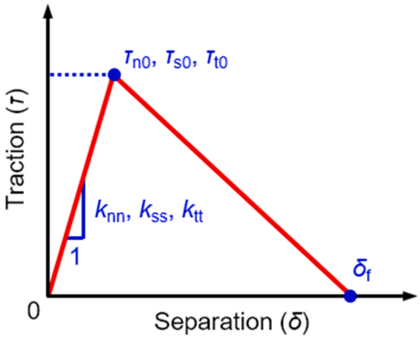

Fig. 15. Traction-separation constitutive law of the ECC/concrete and UHPC/concrete interface.

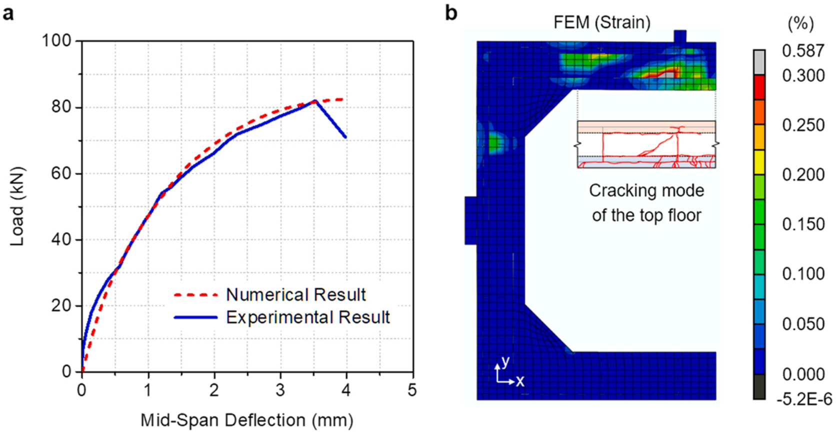

Fig. 16. Results of FE analysis for composite utility tunnel: (a) Mid-span load-deflection curve of top floor and (b) principal strain field at the peak load. The FE results show good agreement with the test results.

8000 N/mm^3, which fell within the suggested range in [56]. τ_{n0}, τ_{s0} and τ_{t0} were assumed to be equal [56] and the value was 22 MPa. These assumptions aimed to achieve a quick convergence in FE analysis.

The results of FE analysis for the composite utility tunnel are presented in Fig. 16. The simulated load vs. mid-span deflection curve of top wall is close to the tested one (Fig. 16**a**). The FE model captures well both the stiffness, strength, and the full-range behaviors. The simulated strain field at the peak load is shown in Fig. 16**b** as compared to the experimentally observed cracking mode of the top wall (i.e., half of Image E in Fig. 8). A significant diagonal crack can be observed in the concrete layer, which coincides with the experimental finding that the failure of the top wall was governed by the shear failure of concrete at the ultimate state (before steel yielding). Additionally, in the FE result, the strain of ECC layer is relatively large at the top wall. It also agrees with the test result that the multi-cracking of ECC layer was observed (see the cracking mode in Fig. 16**b**). The above results indicate that the FE model and the implemented constitutive laws can be applied to predict the mechanical behavior of the UHPC-concrete-ECC composite utility tunnel.

6. Conclusions

The mechanical behavior of UHPC-concrete-ECC composite utility tunnel reinforced by perforated steel plate has been experimentally and numerically investigated. Direct tensile test and DIC analysis have been conducted to understand the composite action between perforated steel plate and ECC. It was found that the in-situ tensile strength of ECC is lower than its material strength, and this needs to be considered for the tensile constitutive model of ECC in FE analysis. The failure of the tested composite utility tunnel was founded to be governed by the shear failure of the concrete layer of the top wall, and the multi-cracking behavior of the ECC layer was observed. According to the DIC result and theoretical estimation, it was found that the crack-control (durability) performance of the composite utility tunnel is superior to that of conventional concrete utility tunnel with the same dimensions and reinforcement ratio, and the composite utility tunnel can be used in severe corrosive environment. The constitutive laws proposed for ECC, UHPC, concrete as well as the interface have been also validated through comparisons between the FE predictions and the experimental load-deflection relations and the failure modes.

This study has demonstrated the potential of the proposed composite utility tunnel in urban underground engineering and provided good knowledge for the design of its short-term mechanical performance. It is noted that the flexural performance of the UHPC-concrete-ECC composite beam reinforced with perforated steel plates can be found in the previous work of the authors [38]. Future studies are needed to verify the fire performance and long-term durability of the UHPC-concrete-ECC composite utility tunnel towards practical applications.

CRediT authorship contribution statement

B.T. Huang: Conceptualization, Methodology, Investigation, Writing – original draft. **J.X. Zhu**: Investigation, Validation, Data curation. **K.F. Weng**: Formal analysis, Software, Writing – review & editing. **J.Q. Huang**: Formal analysis, Software, Writing – review & editing. **J.G. Dai**: Conceptualization, Writing – review & editing, Funding acquisition, Supervision.

Declaration of Competing Interest

The authors declare that they have no known competing financial interests or personal relationships that could have appeared to influence the work reported in this paper.

Acknowledgments

This study was financially supported by the National Key Research Program of China (No.: 2017YFC0703403) and the Research Institute for Sustainable Urban Development, Hong Kong Polytechnic University (No.: 1-BBWE). Bo-Tao Huang would like to acknowledge the support by the Hong Kong Innovation and Technology Fund (No. ITS/077/18FX) through the Research Talent Hub. Jun-Qi Huang acknowledges the financial support by Prefabricated Building Research Institute of Anhui Province (No. AHZ-PY20202KF). The authors also thank Mr. Xiao-Hua Ji, Mr. Xing Yin, and Mr. Hong Li at the College of Civil Engineering and Architecture, Zhejiang University for their support in experiments.

References

[1] United Nations, Department of Economic and Social Affairs, Population Division, World Urbanization Prospects: The 2014 Revision, Highlights (ST/ESA/SER.A/352), United Nations Headquarters, New York, United States, 2014.
[2] J. Canto-Perello, J. Curiel-Esparza, Assessing governance issues of urban utility tunnels, Tunn. Undergr. Space Technol. 33 (2013) 82–87.
[3] T. Wang, L. Tan, S. Xie, B. Ma, Development and applications of common utility tunnels in China, Tunn. Undergr. Space Technol. 76 (2018) 92–106.
[4] GB50838-2015, Technical Code for Urban Utility Tunnel Engineering. Ministry of Housing and Urban-Rural Development of the People's Republic of China, Beijing, China, 2015 (in Chinese).
[5] SJG 32-2017, Technical specification for utility tunnel engineering in Shenzhen, Shenzhen Housing and Construction Bureau, Shenzhen, China, 2017 (in Chinese).
[6] C. Li, Q. Chen, R. Wang, M. Wu, Z. Jiang, Corrosion assessment of reinforced concrete structures exposed to chloride environments in underground tunnels: theoretical insights and practical data interpretations, Cem. Concr. Compos. (2020), 103652.
[7] R. Pan, G. Zhu, Z. Liang, G. Zhang, H. Liu, X. Zhou, Experimental study on the fire shape and maximum temperature beneath ceiling centerline in utility tunnel under the effect of curved sidewall, Tunn. Undergr. Space Technol. 99 (2020), 103304.
[8] V.C. Li, C.K.Y. Leung, Steady-state and multiple cracking of short random fiber composites, J. Eng. Mech. 118 (11) (1992) 2246–2264.

[9] B.T. Huang, J.Q. Wu, J. Yu, J.G. Dai, C.K.Y. Leung, High-strength seawater sea-sand Engineered Cementitious Composites (SS-ECC): mechanical performance and probabilistic modeling, Cem. Concr. Compos. 114 (2020), 103740.
[10] B.T. Huang, K.F. Weng, J.X. Zhu, Y. Xiang, J.G. Dai, V.C. Li, Engineered/strain-hardening cementitious composites (ECC/SHCC) with an ultra-high compressive strength over 210 MPa, Compos. Commun. 26 (2021), 100775.
[11] P. Richard, M. Cheyrezy, Composition of reactive powder concretes, Cem. Concr. Res. 25 (7) (1995) 1501–1511.
[12] K. Wille, S. El-Tawil, A.E. Naaman, Properties of strain hardening ultra high performance fiber reinforced concrete (UHP-FRC) under direct tensile loading, Cem. Concr. Compos. 48 (2014) 53–66.
[13] B.T. Huang, Y.T. Wang, J.Q. Wu, J. Yu, J.G. Dai, C.K.Y. Leung, Effect of fiber content on mechanical performance and cracking characteristics of ultra-high-performance seawater sea-sand concrete (UHP-SSC), Adv. Struct. Eng. 24 (6) (2020) 1182–1195.
[14] J.G. Dai, B.T. Huang, S.P. Shah, Recent advances in strain-hardening UHPC with synthetic fibers, J. Compos. Sci. 5 (10) (2021) 283.
[15] B.T. Huang, J. Yu, J.Q. Wu, J.G. Dai, C.K. Leung, Seawater sea-sand Engineered Cementitious Composites (SS-ECC) for marine and coastal applications, Compos. Commun. 20 (2020), 100353.
[16] D. Zhang, J. Yu, H. Wu, B. Jaworska, B.R. Ellis, V.C. Li, Discontinuous micro-fibers as intrinsic reinforcement for ductile Engineered Cementitious Composites (ECC), Compos. Part B Eng. 184 (2020), 107741.
[17] B.T. Huang, Q.H. Li, S.L. Xu, Fatigue deformation model of plain and fiber-reinforced concrete based on weibull function, J. Struct. Eng. 145 (1) (2019), 04018234.
[18] X. Lin, J. Yu, H. Li, J.Y. Lam, K. Shih, I.M. Sham, C.K. Leung, Recycling polyethylene terephthalate wastes as short fibers in strain-hardening cementitious composites (SHCC), J. Hazard. Mater. 357 (2018) 40–52.
[19] B.T. Huang, Q.H. Li, S.L. Xu, L. Zhang, Static and fatigue performance of reinforced concrete beam strengthened with strain-hardening fiber-reinforced cementitious composite, Eng. Struct. 199 (2019), 109576.
[20] B.T. Huang, Q.H. Li, S.L. Xu, B.M. Zhou, Frequency effect on the compressive fatigue behavior of ultrahigh toughness cementitious composites: experimental study and probabilistic analysis, J. Struct. Eng. 143 (8) (2017), 04017073.
[21] B.T. Huang, Q.H. Li, S.L. Xu, W. Liu, H.T. Wang, Fatigue deformation behavior and fiber failure mechanism of ultra-high toughness cementitious composites in compression, Mater. Des. 157 (2018) 457–468.
[22] J. Zhou, J. Pan, C.K. Leung, Mechanical behavior of fiber-reinforced engineered cementitious composites in uniaxial compression, J. Mater. Civ. Eng. 27 (1) (2014), 04014111.
[23] J. Yu, H.L. Wu, C.K. Leung, Feasibility of using ultrahigh-volume limestone-calcined clay blend to develop sustainable medium-strength Engineered Cementitious Composites (ECC), J. Clean. Prod. (2020), 121343.
[24] B.T. Huang, Q.H. Li, S.L. Xu, B.M. Zhou, Tensile fatigue behavior of fiber-reinforced cementitious material with high ductility: experimental study and novel *P-S-N* model, Constr. Build. Mater. 178 (2018) 349–359.
[25] Y. Yang, M.D. Lepech, E.H. Yang, V.C. Li, Autogenous healing of engineered cementitious composites under wet–dry cycles, Cem. Concr. Res. 39 (5) (2009) 382–390.
[26] Z. Zhang, Q. Zhang, Self-healing ability of engineered cementitious composites (ECC) under different exposure environments, Constr. Build. Mater. 156 (2017) 142–151.
[27] B.T. Huang, J.Q. Wu, J. Yu, J.G. Dai, C.K. Leung, V.C. Li, Seawater sea-sand engineered/strain-hardening cementitious composites (ECC/SHCC): assessment and modeling of crack characteristics, Cem. Concr. Res. 140 (2021), 106292.
[28] C. Wu, Z. Pan, R.K.L. Su, C.K. Leung, S. Meng, Seismic behavior of steel reinforced ECC columns under constant axial loading and reversed cyclic lateral loading, Mater. Struct. 50 (1) (2017) 78.
[29] Y. Alrefaei, K. Rahal, M. Maalej, Shear strength of beams made using hybrid fiber–engineered cementitious composites, J. Struct. Eng. 144 (1) (2018), 04017177.
[30] B.T. Huang, Q.H. Li, S.L. Xu, B. Zhou, Strengthening of reinforced concrete structure using sprayable fiber-reinforced cementitious composites with high ductility, Compos. Struct. 220 (2019) 940–952.
[31] J. Cai, J. Pan, J. Tan, X. Li, Bond behaviours of deformed steel rebars in engineered cementitious composites (ECC) and concrete, Constr. Build. Mater. 252 (2020), 119082.
[32] E. Mündecke, V. Mechtcherine, Tensile behaviour of strain-hardening cement-based composites (SHCC) with steel reinforcing bars, Cem. Concr. Compos. 105 (2020), 103423.
[33] M. Sahmaran, M. Lachemi, V.C. Li, Assessing mechanical properties and microstructure of fire-damaged engineered cementitious composites, Acids Mater. J. 107 (3) (2010) 297.
[34] M. Sahmaran, E. Özbay, H.E. Yücel, M. Lachemi, V.C. Li, Effect of fly ash and PVA fiber on microstructural damage and residual properties of engineered cementitious composites exposed to high temperatures, J. Mater. Civ. Eng. 23 (12) (2011) 1735–1745.
[35] K.Q. Yu, J.G. Dai, Z.D. Lu, C.K. Leung, Mechanical properties of engineered cementitious composites subjected to elevated temperatures, J. Mater. Civ. Eng. 27 (10) (2014), 04014268.
[36] T/CBMF 37-2018, T/CCPA 7-2018, Fundamental characteristics and test methods of ultra-high performance concrete. China Construction Material Federation, China Concrete & Cement-based Products Association, 2018 (in Chinese).
[37] J.G. Teng, Y. Xiang, T. Yu, Z. Fang, Development and mechanical behaviour of ultra-high-performance seawater sea-sand concrete, Adv. Struct. Eng. 22 (14) (2019) 3100–3120.
[38] B.T. Huang, J.G. Dai, K.F. Weng, J.X. Zhu, S.P. Shah, Flexural performance of UHPC-concrete-ECC composite member reinforced by perforated steel plate, J. Struct. Eng. 147 (6) (2020), 04021065.
[39] GB50009-2019, Load Code for the design of building structures. Ministry of Housing and Urban-Rural Development of the People's Republic of China, Beijing, China, 2019 (in Chinese).
[40] L.Y. Xu, B.T. Huang, J.G. Dai, Development of engineered cementitious composites (ECC) using artificial fine aggregates, Constr. Build. Mater. 305 (2021), 124742.
[41] L.Y. Xu, B.T. Huang, V.C. Li, J.G. Dai, High-strength high-ductility Engineered/Strain-Hardening Cementitious Composites (ECC/SHCC) incorporating geopolymer fine aggregates, Cem. Concr. Compos. 125 (2022), 104296.
[42] B.T. Huang, Q.H. Li, S.L. Xu, C.F. Li, Development of reinforced ultra-high toughness cementitious composite permanent formwork: experimental study and digital image correlation analysis, Compos. Struct. 180 (2017) 892–903.
[43] Q.H. Li, X. Yin, B.T. Huang, A.M. Luo, Y. Lyu, C.J. Sun, S.L. Xu, Shear interfacial fracture of strain-hardening fiber-reinforced cementitious composites and concrete: a novel approach, Eng. Fract. Mech. 253 (2021), 107849.
[44] GOM, GOM Correlate Professional Manual Basic, GOM mbH, Germany, 2015.
[45] Chinese standard GB50010-2010, Code for design of concrete structures. Ministry of Housing and Urban-Rural Development of the People's Republic of China, Beijing, China, 2010.
[46] ABAQUS, ABAQUS Standard User's Manual. Hibbitt, Karlsson & Sorensen, 2010.
[47] M. Safdar, T. Matsumoto, K. Kakuma, Flexural behavior of reinforced concrete beams repaired with ultra-high performance fiber reinforced concrete (UHPFRC), Compos. Struct. 157 (2016) 448–460.
[48] E.H. Yang, S. Wang, Y. Yang, V.C. Li, Fiber-bridging constitutive law of engineered cementitious composites, J. Adv. Concr. Technol. 6 (1) (2008) 181–193.
[49] J. Yu, C. Lu, Y. Chen, C.K. Leung, Experimental determination of crack-bridging constitutive relations of hybrid-fiber strain-hardening cementitious composites using digital image processing, Constr. Build. Mater. 173 (2018) 359–367.
[50] AFGC (Association Française du Génie Civil), Bétons fibrés à ultra-hautes performances (Ultra high performance fibre-reinforced concretes), SETRA – Service d'études techniques des routes et autoroutes, AFGC, France, 2013,152.

[51] A.S. Genikomsou, M.A. Polak, Finite element analysis of punching shear of concrete slabs using damaged plasticity model in ABAQUS, Eng. Struct. 98 (2015) 38–48.
[52] J.Q. Huang, J.G. Dai, Flexural performance of precast geopolymer concrete sandwich panel enabled by FRP connector, Compos. Struct. 248 (2020), 112563.
[53] J.Q. Huang, J.G. Dai, Direct shear tests of glass fiber reinforced polymer connectors for use in precast concrete sandwich panels, Compos. Struct. 207 (2019) 136–147.
[54] M.K.I. Khan, C.K. Lee, Y.X. Zhang, Numerical modelling of engineered cementitious composites-concrete encased steel composite columns, J. Constr. Steel Res. 170 (2020), 106082.
[55] M.H. Mollazadeh, Y.C. Wang, New insights into the mechanism of load introduction into concrete-filled steel tubular column through shear connection, Eng. Struct. 75 (2014) 139–151.
[56] Y. Zhu, Y. Zhang, H.H. Hussein, G. Chen, Numerical modeling for damaged reinforced concrete slab strengthened by ultra-high performance concrete (UHPC) layer, Eng. Struct. 209 (2020), 110031.